Structure evolution of Na_2O_2 from room temperature to 500 ºC

Chun-Hai Wang[1, 2, *], Dong-Yun Gui[3], Qingbo Xia[2], Maxim Avdeev[2,4], Chris D Ling[2] and Brendan J Kennedy[2,*]

[1] State Key Laboratory of Solidification Processing, Northwestern Polytechnical University, Xi'an, Shaanxi 710072, China

[2] School of Chemistry, The University of Sydney, Sydney NSW 2006, Australia

[3] Institute of Functional Materials, College of Materials Science and Engineering, Xi'an University of Architecture and Technology

[4] Australian Centre for Neutron Scattering, Australian Nuclear Science and Technology Organisation, Menai NSW 2234, Australia

Abstract

Na_2O_2 is one of the possible discharge products from sodium-air batteries. Here we report the evolution of the structure of Na_2O_2 from room temperature to 500 ºC using variable-temperature neutron and synchrotron X-ray powder diffraction. A phase transition from α-Na_2O_2 to β-Na_2O_2 is observed in the neutron diffraction measurements above 400 ºC and the crystal structure of β-Na_2O_2 is determined from neutron diffraction data at 500 ºC. α-Na_2O_2 adapts a hexagonal $P\bar{6}2m$ (No. 189) structure and β-Na_2O_2 adapts a tetragonal $I4_1/acd$ (No. 142) structure. The thermal expansion coefficients of α-Na_2O_2 is $a = 2.98\times10^{-5}$ K^{-1}, $c = 2.89\times10^{-5}$ K^{-1} and $V = 8.96\times10^{-5}$ K^{-1} up to 400 ºC and a ~10% volume expansion occurs during the phase transition from α-Na_2O_2 to β-Na_2O_2 due to the re-alignment/rotation of O_2^{2-} groups. Both phases are electronic insulators according to DFT calculations with band gaps (both indirect) of 1.75 eV (α-Na_2O_2) and 2.56 eV (β-Na_2O_2). Impedance analysis from room temperature to 400 ºC revealed a significant enhancement of conductivity at $T \geq 275$ ºC. α-Na_2O_2 shows higher conductivity (~10 times at $T \leq 275$ ºC and ~3 times at $T > 275$ ºC) in O_2 compared to in Ar. We confirmed, by dielectric analysis, that this enhanced conductivity is dominated by ionic conduction.

Introduction

Electrical energy storage is a global concern and great efforts are being directed towards the development of new improved batteries and related technologies. There is a limited variety of rechargeable batteries in wide scale use, notably lithium-ion batteries, lead-acid batteries and sodium-sulphur batteries [1]. As global demand increases and the limitations of the existing batteries in terms of adverse environmental impact, safety, cost, and power density become more apparent, there is a great impetus to develop new classes of batteries. Sodium-based batteries (sodium-air or sodium ion) [2] are promising due to the lower cost and larger natural abundance of sodium compared to lithium. Sodium-air batteries, in particular, are attracting attention due to

* Corresponding author, CHW: chwang81@gmail.com; BJK: brendan.kennedy@sydney.edu.au

their high theoretical specific energy. For example, the theoretical energy density of a Na/O_2 cell is 1600 Wh/kg with Na_2O_2 as a discharge product [3]. However, limited battery lifetime and poor rechargeability are bottlenecks to the commercialisation of sodium-air batteries. Both the lifetime and rechargeability are mainly controlled by the stability and transport behaviour of the discharge products. Thus, detailed investigations of the key properties including crystal structure, thermal behaviour, dynamics, etc. of the discharge products are needed to develop and commercially deploy sodium-air batteries.

The discharge products of sodium-air batteries are expected to be one or more of the Na-O 'oxide' phases. There are four 'oxide' compositions reported in the Na-O system to date[4]: sodium oxide Na_2O [5], sodium peroxide Na_2O_2 [6, 7], sodium superoxide NaO_2 [8, 9] and sodium ozonide NaO_3 [10]. Among these, Na_2O_2 (or $Na_2O_2{\bullet}2H_2O$) and NaO_2 are the main discharge products observed [11-16] in state-of-the-art sodium-air batteries. Therefore, improved understanding of the structures of these species and related properties is necessary.

The availability of precise and accurate crystal structures is important for the development and theoretical modelling of materials. The crystal structure of α-Na_2O_2 was determined by Tallman *et al*. almost 60 years ago using single crystal X-ray diffraction measurements. They reported that α-Na_2O_2 adapts a hexagonal unit cell $P\bar{6}2m$ (No. 189) with a = 6.208 Å, c = 4.469 Å [6]. The structure of Na_2O_2 at room temperature (Na_2O_2-I or α-Na_2O_2) is shown in Figure 1 [6]. In this structure the oxygen atoms are present as O_2^{2-} peroxide ions parallel to c axis. Tallman and Margrave [7] observed another phase, Na_2O_2-II, at temperatures above 510 ºC and a third phase, Na_2O_2-Q, from liquid-air quenched molten Na_2O_2. However, the crystal structures of neither Na_2O_2-II nor Na_2O_2-Q have been reported to date.

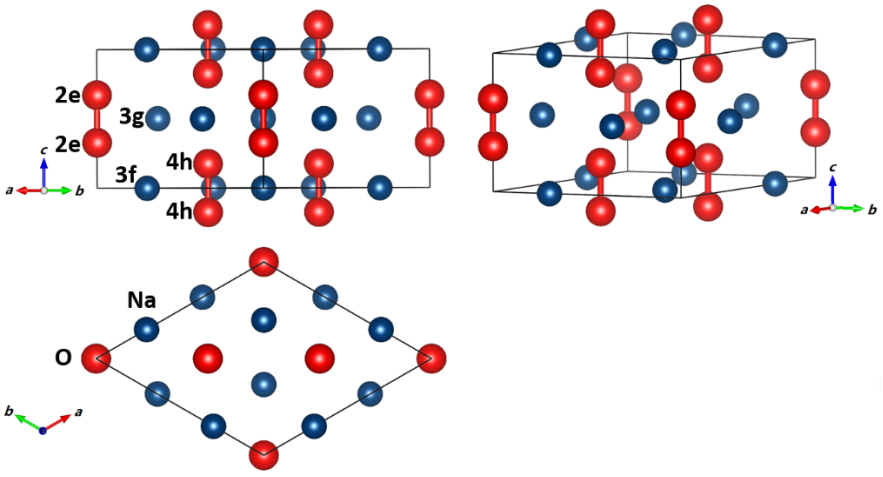

Figure 1. Representations of the structure of α-Na_2O_2 highlighting the arrangement of the O_2^{2-} peroxide groups. The Wykoff positions are indicated.

Yang and Siegel[15] studied the intrinsic conductivity of α-Na_2O_2 by density functional theory (DFT) and (GW) many-body perturbation method calculations. They predicted that it would have low electrical conductivity

(~10^{-20} S/cm at room temperature) due to sluggish charge-hopping between $[O_2]^{2-}$ dimers, and that the ionic conductivity (primarily due to *n*-type sodium vacancies or/and *p*-type $[O_2]^{2-}$ dimer vacancies) should be ten orders of magnitude larger. Araujo *et al*.[17] also used DFT to investigate charge migration in α-Na_2O_2 and found that the conductivity is dominated by the diffusion of hole polarons. These results are consistent with the experimental studies of Dunst *et al*.[18] and Philipp *et al*.[19] who independently investigated the temperature-dependent conductivity of α-Na_2O_2. Dunst *et al*.[18] observed an electronic conductivity around 10^{-14} S/cm at room temperature and an activation energy from 193 to 373 K of ~1.06 eV. Philipp *et al*. [19] observed a similar activation energy and a strong coupling between Na^+ ionic transport and electronic dynamics.

In the present work we report the temperature-dependent crystal structure and conductivity of Na_2O_2 studied using high-resolution synchrotron X-ray, neutron powder diffraction and impedance analysis respectively. We also describe the crystal structure of Na_2O_2-II (β-Na_2O_2) refined against neutron powder diffraction data.

Experimental section and calculation details

Sample. Sodium peroxide Na_2O_2 was obtained from Alfa Aesar®. The pale yellow granular solid was ground using an agate mortar and pestle in a glovebox (Ar filled, O_2 < 5 ppm and H_2O < 1 ppm) before use. It should be noted that Na_2O_2 is a strong oxidiser and extreme caution should be exercised during handling. Na_2O_2 reacts dramatically with silica or metal containers at temperatures higher than 500 ºC. It is also moisture-sensitive and should be handled in a moisture-free glovebox.

Synchrotron X-ray diffraction measurements. The well-ground Na_2O_2 powder was loaded into a 1 mm diameter capillary and sealed in the glovebox before measurements. Synchrotron X-ray diffraction data (syn-XRD) were collected on the Powder Diffraction beamline at the Australian Synchrotron [20]. The data (Debye-Scherrer method) were collected using an array of Mythen microstrip detectors from 5º to 76.5º 2θ with X-rays of wavelength λ = 0.827052(1) Å, which covers the *d*-spacing range 9.48033 – 0.66795 Å. To cover the gaps between individual detector modules, two data sets were collected with the detector offset by 0.5º and then merged to a single data set using the PDViPeR software. Variable-temperature (VT) diffraction data were collected from room temperature to 500 ºC.

Neutron diffraction measurements. Powder neutron diffraction (ND) data were collected on the high-resolution powder diffractometer ECHIDNA [21] at the OPAL research reactor, ANSTO, Australia. A ~4 g well-ground Na_2O_2 sample was loaded into a 6 mm diameter vanadium can and sealed in the glovebox before the measurements. The ND data were collected from room temperature to 500 ºC, using neutrons of wavelength λ = 1.6215 Å over a 15–160 º2θ range (corresponding to a *d*-spacing range 6.2114–0.8233 Å).

Impedance analysis. The conductivity of Na_2O_2 was investigated using an MTZ-35 impedance analyzer (Bio-Logic). Approximately 0.33 g of well-ground Na_2O_2 were pressed into a pellet at ~400 MPa (~80% relative density achieved as Na_2O_2 are soft) and loaded into a HTSH-1100 high-temperature sample holder between two Φ13mm platinum plate electrodes (Bio-Logic) in the glovebox. Variable-temperature measurements from

50 ºC to 400 ºC (Na_2O_2 reacts with the metal electrode at temperature higher than 400 ºC) were then conducted under high-purity O_2 or Ar, dried by passing through condensed (98%) H_2SO_4 added with P_2O_5 to improve the drying capacity. The alternating (AC, 0.5 V) sweeping range was selected as 0.1 to 1×10^6 Hz.

Structure refinement. The structure of α-Na_2O_2 was investigated by Rietveld refinements against syn-XRD and ND data measured at the same temperatures. TOPAS Academic (TA)[22, 23] was employed during the Rietveld refinements and an intensity weighting (10%) was applied to the syn-XRD data to keep a reasonable weighting for both the syn-XRD and ND data during the refinement. The ND data collected at 500 ºC were used to establish the structure of β-Na_2O_2. The structure was solved using Jana2006 [24] and ultimately refined using TOPAS Academic (TA). All crystal structure visualization was done using the program VESTA [25].

Band structure calculations. The band structure of Na_2O_2 was calculated using the CASTEP (Cambridge Serial Total Energy Package) DFT software-package [26]. A plane-wave basis set with a cut-off energy E_{cut} = 660 eV was chosen for expansion of valence-electron wave functions and PBE gradient-corrected functionals (GGA) for solid/surface (PBEsol) [27] were selected. The structures obtained experimentally in the current work were selected and then optimized. The k-space was sampled using a Monkhorst-Pack grid with reciprocal spacing ~ 0.03 $Å^{-1}$ and the ultrasoft pseudopotential was constructed from the CASTEP database. The criterion for self-consistency (SCF) was eigenenergy convergence within 10^{-8} eV/atom.

Results and discussions

Phase and structure of α-Na_2O_2. The ND and syn-XRD patterns of α-Na_2O_2 measured at room temperature are shown in Figure 2. Rietveld-refinement against the combined ND and syn-XRD data sets was performed and an excellent fit (overall R_{wp} = 0.043) achieved. Due to the different atomic scattering factors (contrast of atoms in structure determinations) of neutron [Na: 3.63(2) fm, O: 5.803(4) fm][28] and X-rays (proportional to elections, Na^+: 10, O^-: 9), the use of the combined data set exploited the differences in the relative X-ray and neutron scattering factors and provided sensitivity to small changes in the lattice parameters and isotropic atomic displacement parameters (ADPs, U_{iso}), yielding a more accurate structural model. The high purity of the Na_2O_2 sample was also confirmed from the refinement. The refined cell parameters of α-Na_2O_2 are given in Table 1 and a crystallographic information file (CIF) is available as supplementary information (SI). The refined cell parameters *a* and *c* are slightly smaller (~0.2%) than reported in Tallman's earlier work (*a* = 6.208 Å, *c* = 4.469 Å)[6]. There are two crystallographically unique Na^+ cations and two O_2^{2-} dimers in the structure. Both Na^+ cations are six coordinated, Na-O distances in Na(1) of 4 × 2.307(1) Å and 2 × 2.371(1) Å, which are noticeably smaller than the distance in Na(2) of 4 × 2.387(1) Å and 2 × 2.450(1) Å. Both O_2^{2-} dimers are six coordinated and the O-O bond lengths of O_2^{2-} dimers are 1.527(1) Å for O(1)-O(1) and 1.556(1) Å for O(2)-O(2).

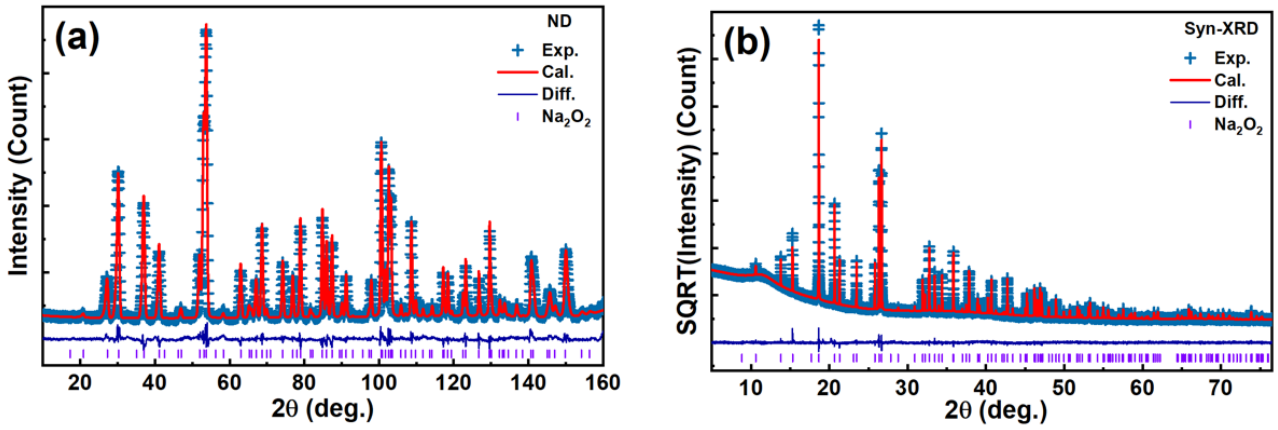

Figure 2. Rietveld-refinement profiles of α-Na_2O_2 at room temperature. Left: ND (wavelength: 1.6215 Å, R_{wp}: 0.048); right: syn-XRD (wavelength: 0.827052 Å, R_{wp}: 0.032); Cross points, observed; solid line, calculated curve; solid line below the data is the difference curve; vertical tick marks, peak positions. Note: the intensity of syn-XRD data is plotted on a square-root scale to enhance the contrast of weak reflections.

Table 1. Structure parameters of α-Na_2O_2 from combined refinement and DFT optimisation

	Experiment (Rietveld refinement)			DFT optimisation
T	RT (295 K)			0 K
a (Å)	6.19270(2)			6.19604
c (Å)	4.46042(2)			4.44626
V (Å^3)	148.138(1)			147.827
Space group	$P\bar{6}2m$ (No. 189)			
Atom	Site	Coordinate	U_{iso} (Å^2)	Coordinate
Na1	$3f$ (x_1, 0, 0)	x_1 = 0.30049(12)	0.0138(2)	x_1 = 0.299456
Na2	$3g$ (x_2, 0, 1/2)	x_2 = 0.63426(12)	0.0142(2)	x_2 = 0.633673
O1	$2e$ (0, 0, z_1)	z_1 = 0.6712(2)	0.0109(1)	z_1 = 0.670035
O2	$4h$ (1/3, 2/3, z_2)	z_2 = 0.17453(13)	0.0100(1)	z_2 = 0.171853

ND and syn-XRD patterns of Na_2O_2 measured from RT to 500 ºC are shown in Figure S1 and S2 of the Supporting Information (SI). The temperature-dependent diffraction intensities over selected 2θ ranges are shown as contour images in Figure 3. The ND profiles reveal that the α-Na_2O_2 to β-Na_2O_2 structural phase transition begins at ~ 400 ºC and finishes at 500 ºC. The phase transition temperature observed in the VT ND measurement is slightly lower than that reported by Tallman *et al.* (510 ºC) [6], which possibly reflects the use of a vacuum-furnace for the ND measurements. Indeed, the phase transition was not observed in the VT syn-XRD measurements up to 500 ºC, where the sample was contained in a sealed capillary. The impact of sample atmosphere on phase transitions is well-documented: see, for example, our recent study of the phase transition

in $SrUO_4$[29]. The fact that Na_2O_2 reacts with silica above 500 ºC precluded X-ray measurements at higher temperatures.

Unit cell parameters of α-Na_2O_2 obtained by Rietveld refinement against the syn-XRD data are plotted in Figure 4. α-Na_2O_2 exhibits nearly isotropic positive thermal expansion from RT to 400 ºC, the average thermal expansion coefficients being $2.98(1)\times10^{-5}$ K^{-1} in *a*, $2.89(1)\times10^{-5}$ K^{-1} in *c* and $8.96(1)\times10^{-5}$ K^{-1} in *V*. This results in a small decrease in the *c*/*a* ratio upon heating. The ADPs for both the Na and O ions increase as the temperature increases, as expected from the enhanced thermal vibration of the atoms at high temperatures.

ND data were collected at fewer temperatures than syn-XRD data. The structures refined against combined ND and syn-XRD at the same temperatures are given in the CIF files of the SI. By virtue of the unambiguous structure determination in the combined refinements, more accurate and precise bond lengths *L* of the O_2^{2-} peroxide ions were obtained, as shown in Figure 5. The O–O bond length of the O_2^{2-} peroxide ions for O1 at the 2*e* site shows an unusual contraction at temperatures above 250 ºC, whereby *L*[O1–O1] decreases from 1.522(2) Å at RT to 1.494(4) Å at 400 ºC. However, the O–O bond length for O2 at the 4*h* site is only weakly temperature-dependent, *L*[O2–O2] remaining essentially constant from 1.557(1) Å at RT to 1.559(2) Å at 400 ºC. The appearance *L*[O1–O1] decreases is possible a librational vibration of O1–O1 dimmer as observed in many negative thermal expanding systems.

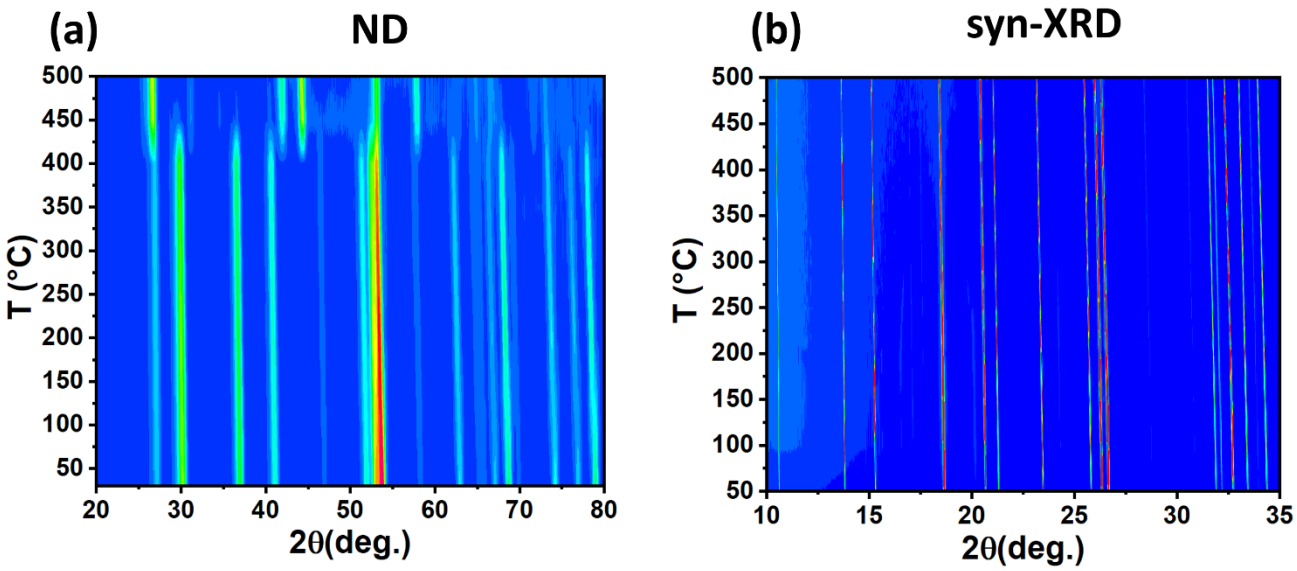

Figure 3. Temperature-dependent ND (wavelength: 1.6215 Å) and syn-XRD (wavelength: 0.827052 Å) of Na_2O_2.

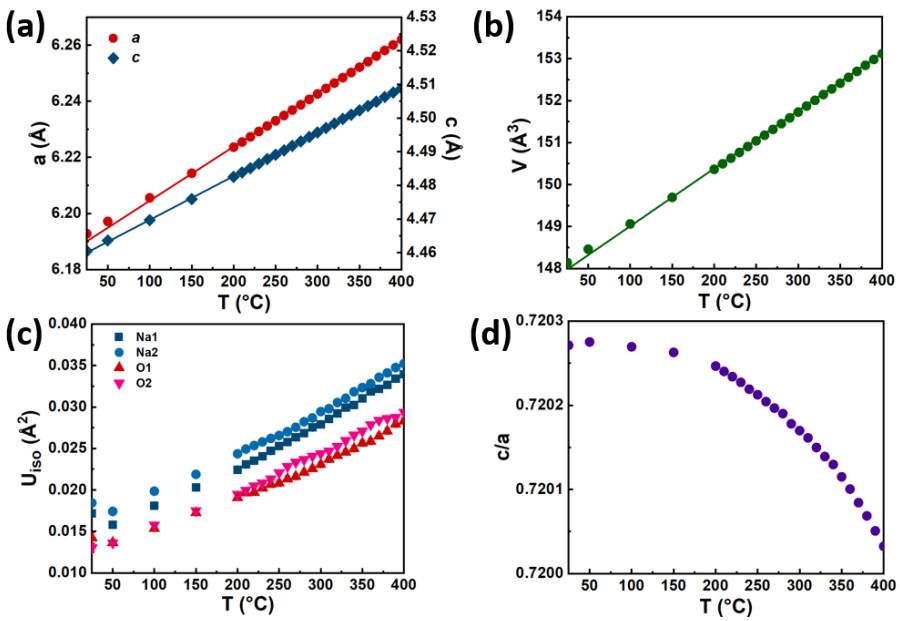

Figure 4. Temperature-dependent unit cell parameters *a*, *c*, *c*/*a*, cell volume *V*, and thermal displacement parameter of *α*-Na_2O_2 from syn-XRD measurements. Where not apparent, the esds are smaller than the size of the symbol.

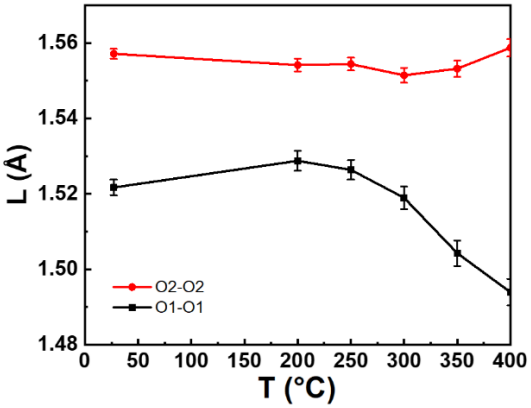

Figure 5. Temperature-dependent O_2^{2-} bond length of *α*-Na_2O_2 from refinement against combined ND and syn-XRD data. O1 2*e* (0, 0, z_1) and O2 4*h* (1/3, 2/3, z_2).

Crystal structure of β-Na_2O_2. Our ND data demonstrate that the *α*-Na_2O_2 to *β*-Na_2O_2 transition is complete by 500 ºC. Consequently, the crystal structure of *β*-Na_2O_2 was solved using the 500 ºC dataset. The ND data at 500 ºC could be indexed by a tetragonal unit cell (from Pawley refinement, Figure S3 in SI): a = 6.1030(2) Å, c = 12.1005(6) Å, V = 450.71(4) Å^3, space group $I4_1/acd$ (No. 142). Using charge-flipping analysis and Rietveld refinement, the crystal structure of *β*-Na_2O_2 was obtained. The crystal structure and refinement profiles are shown in Figure 6. The quality of the refinement of *β*-Na_2O_2 is lower than that obtained using the RT data (R_{wp} = 0.066 vs 0.043). This should be related to texture in the sample. The refined cell parameters of *β*-Na_2O_2 are given in Table 1 and a CIF is available in the SI. The cell contents of *β*-Na_2O_2 are $Na_{16}O_{16}$ (Z = 8) and *β*-Na_2O_2 is isostructural to tetragonal Na_2C_2 reported by Hemmersbach *et al.* [30] The O_2^{2-} dimers lies in *a*-*b*

plane with the O-O bond length 1.557(8) Å, which is similar to *L*[O2–O2] in α-Na_2O_2. The Na-O bond lengths of Na-O 2 × 2.351(5) Å, 2 × 2.368(3) Å and 2 × 2.606(2) Å are typical of NaO_6 octahedra. The local chemical environment (first coordination shell) of the O_2^{2-} dimer and Na^+ is shown in Figure 7(a). Each O_2^{2-} dimer coordinates to eight Na^+, and each Na^+ coordinates to six oxygen atoms from four O_2^{2-} dimers. The ND pattern of Na_2O_2 sample at 450 ºC with α-Na_2O_2 and β-Na_2O_2 co-exist is given as Figure S4 in SI. The Rietveld and Pawley refined profiles are also shown. Cell parameters of β-Na_2O_2 at 450 ºC from Pawley refinement are a = 6.0928(3) Å, c = 12.0860(6) Å, V = 448.66(4) Å^3 and the thermal expansion coefficients of β-Na_2O_2 are estimated as 3.35(1)×10^{-5} K^{-1} in a, 2.40(1)×10^{-5} K^{-1} in c and 9.14(1)×10^{-5} K^{-1} in V.

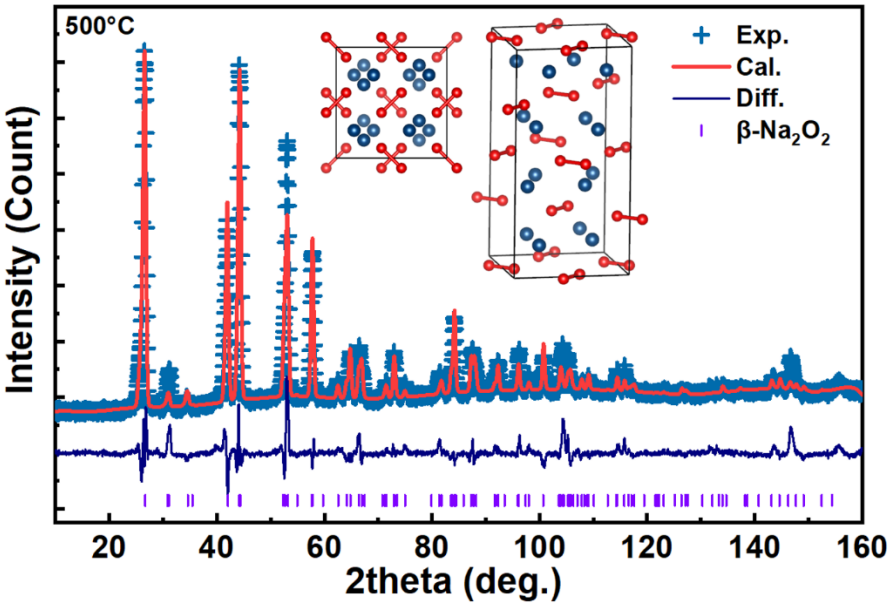

Figure 6. Rietveld-refinement profiles of β-Na_2O_2 against ND data at 500 °C (wavelength: 1.6215 Å, R_{wp}: 0.066). Cross points, observed; red solid line, calculated curve; solid line below the data is the difference curve; vertical tick marks, peak positions. The crystal structure of β-Na_2O_2 is shown in the inset (red ball: O, navy ball: Na).

Table 2. Structure parameters of β-Na_2O_2 from refinement against ND data and DFT optimization.

	Experiment (Rietveld refinement)			DFT optimisation
T	500 ºC (773 K)			0 K
a (Å)	6.1046(4)			5.95984
c (Å)	12.0972(10)			11.9221
V (Å^3)	450.82(7)			423.468
Space group	*I*4$_1$/*acd* (No. 142)			
Atom	Site	Coordinate	U_{iso} (Å^2)	Coordinate
Na1	*16e* (1/4, *y*, 1/8)	*y* = 0.3380(8)	0.063(1)	*y* = 0.34218

O1	16*f* (*x*, *x*, 1/4)	*x* = 0.0902(2)	0.053(1)	*x* = 0.08953

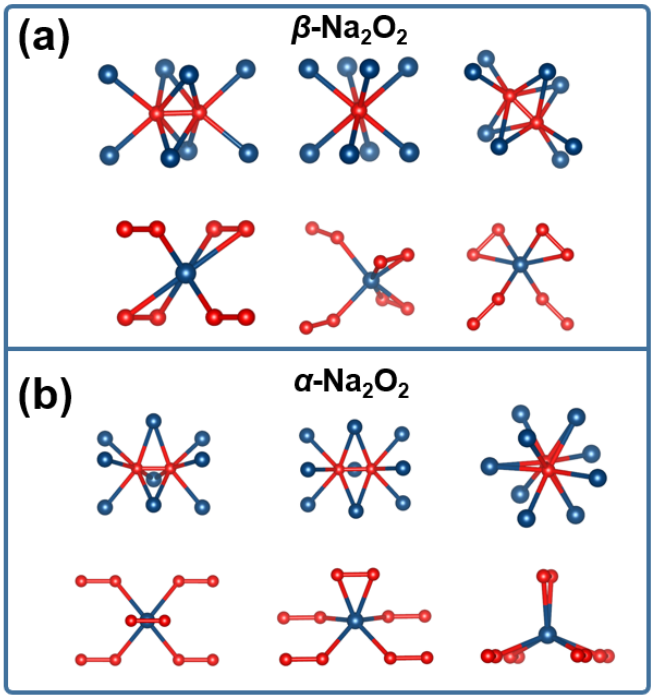

Figure 7. The coordination environments of O_2^{2-} and Na^+ in β-Na_2O_2 (a) and α-Na_2O_2 (b) viewed from different directions. (Red ball: O, navy ball: Na)

Comparison of α-Na_2O_2 and β-Na_2O_2. The phase transition from α-Na_2O_2 to β-Na_2O_2 is required to be first-order by symmetry and this is evident from the co-existence of the two phases observed in the ND data around 450 ºC. The transition involves a reorientation of the O_2^{2-} groups from along a single direction in α-Na_2O_2 to about two perpendicular directions in β-Na_2O_2. The first coordination shells of the O_2^{2-} and Na^+ ions in α-Na_2O_2 are shown in Figure 7(b). As observed in α-Na_2O_2 each Na^+ is six-coordinate (involving five O_2^{2-} dimers) whilst the coordination number (CN) of each O_2^{2-} moiety is nine which is larger than that of β-Na_2O_2. In α-Na_2O_2, the average Na-O and O-O bond length are 2.368(1) Å and 1.542(2) Å. In β-Na_2O_2, the average Na-O and O-O bond length are 2.442(3) Å and 1.557(8) Å, which are longer than that of α-Na_2O_2. Thus, the crystal structure of β-Na_2O_2 can be considered as less tightly packed than α-Na_2O_2. The calculated density of β-Na_2O_2 at 500 ºC is 2.298(4) g/cm^3, while α-Na_2O_2 has a density of 2.622(1) g/cm^3 at room temperature that decreases slightly to 2.537(1) g/cm^3 at 400 ºC, which means a ~10% volume expansion occurs during the phase transition from α-Na_2O_2 to β-Na_2O_2.

Conductivity of α-Na_2O_2. Nyquist plots (Z''-Z' plot) of the impedance spectra of α-Na_2O_2 at different temperatures, measured under either Ar or O_2 atmospheres, are shown in Figure S5 of the SI. The temperature-dependent conductivity is plotted in Figure 8, which shows that α-Na_2O_2 has higher conductivity (~10 times at $T \leq 275$ ºC and ~3 times at $T > 275$ ºC) in O_2 than in Ar. For both atmospheres there is a

progressive increase in conductivity as the temperature is increased from 100 ºC to 250 ºC, above which there is a dramatic reversible increase in conductivity (0.03–0.09 S/cm in O_2) irrespective of the atmosphere. The possibility that this increase is related to the presence of hydroxide impurities cannot be totally excluded, but the absence of any spurious peaks in the syn-XRD data and the absence of any background anomalies in the ND data argue against this. Further studies of the conductivity mechanism are planned. Conductivity of α-Na_2O_2 here is a bit lower than that of nanocrystalline α-Na_2O_2 reported by Dunst *et al.*[18] (3.5×10^{-10} S/cm versus ~6×10^{-10} S/cm at 100 ºC) due to different sample status. The activation energy in α-Na_2O_2, estimated assuming an Arrhenius relationship, is E_a = 1.7(3) eV at T < 275 ºC and E_a = 1.04(3) eV at $T \geq$ 275 ºC in Ar, E_a = 1.91(8) eV at T < 275 ºC and E_a = 0.95(7) eV at $T \geq$ 275 ºC in O_2. The activation energy here is higher than that reported by Dunst *et al.*[18] (1.01 - 1.06 eV at -80 - 100 ºC). Besides of the different sample (normal powder against nanocrystalline) origin, the charge carrier might not follow an ideal Arrhenius relationship due to a complex charge carrier interaction (coupling). Due to the high conductivity of the sample, an inductor effect from the cables is evident as a high frequency tail in the Nyquist plots (Figure S5 and a quick equivalent circuit fit in Figure S6). The temperature-dependent relative dielectric constant ε_r (real part and imaginary part, $\varepsilon_r^* = \varepsilon_r' - j\varepsilon_r''$) plots of α-Na_2O_2 are shown in Figure 9. The dielectric constant increases by several orders of magnitude over the frequency range 10^6 Hz to 10^{-1} Hz, with the increase being most noticeable for $T \geq$ 275 ºC. For example, a colossal dielectric constant $\varepsilon_r' \approx 10^{11}$ and $\varepsilon_r'' \approx 10^{12}$ was observed at 10^{-1} Hz for Na_2O_2 in O_2 at 400 ºC. This anomalously high dielectric constant is similar to that reported for $Rb_2Ti_2O_5$ [31] by Federicci *et al*. The high dielectric constant suggests a high polarisation, which should be a result of macroscopic ion displacement (migration).

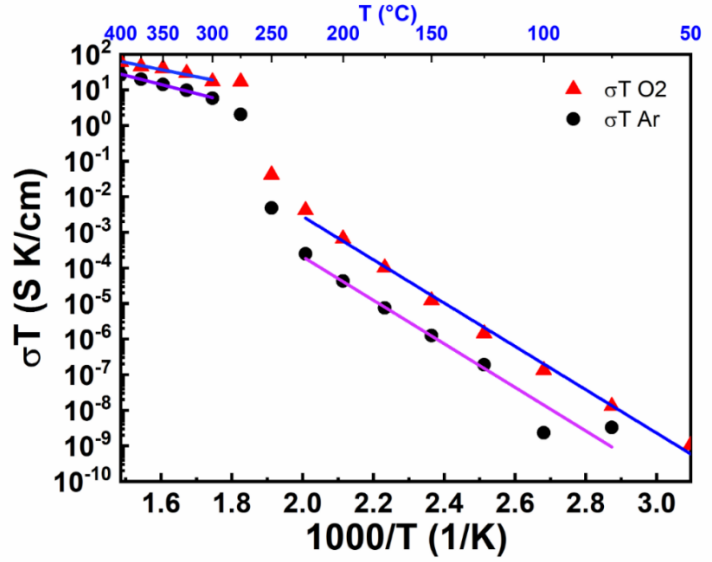

Figure 8. Temperature-dependent conductivity of α-Na_2O_2.

DFT calculations. The details of the crystal structures of α-Na_2O_2 and β-Na_2O_2 after DFT geometry optimizations are included in Table 1 and Table 2. The optimised structures agree reasonably well with the

experimentally observed structures. The slightly smaller unit cell of β-Na_2O_2 from DFT optimisation might be caused by the absence of thermal vibrations at the effective calculation temperature of 0 K and errors from DFT approximations. The system energy of α-Na_2O_2 is slightly lower (–0.047 eV per Na_2O_2, ~ –4.54 kJ/mol) than that of β-Na_2O_2, which agrees with the observed phase stability at room temperature. According to the band structure obtained from the DFT calculations (see Figure S7 in SI), both α-Na_2O_2 and β-Na_2O_2 are indirect electronic insulators. α-Na_2O_2 shows an indirect band gap E_g(i) = 1.83 eV (Γ→A) and a direct band gap E_g(d) = 2.28 eV (A→A). Both these are larger in β-Na_2O_2 which has an indirect band gap E_g(i) = 2.56 eV and a direct band gap E_g(d) = 2.65 eV. In general, DFT calculations underestimate the band gaps of solids [32, 33], therefore the real band gap of Na_2O_2 might be larger. Indeed, Yang and Siegel [15] recently calculated the band structure of α-Na_2O_2 using three different methods (GGA, HSE06, and HSE+G_0W_0) and concluded that the G_0W_0 calculations provided the best estimate of the true bandgap as 6.65 eV[15]. The activation energy in α-Na_2O_2 from conductivity measurements are smaller than the band gap confirms that the conductivity observed here (especially for $T \geq 275$ ºC) is predominantly ionic in origin.

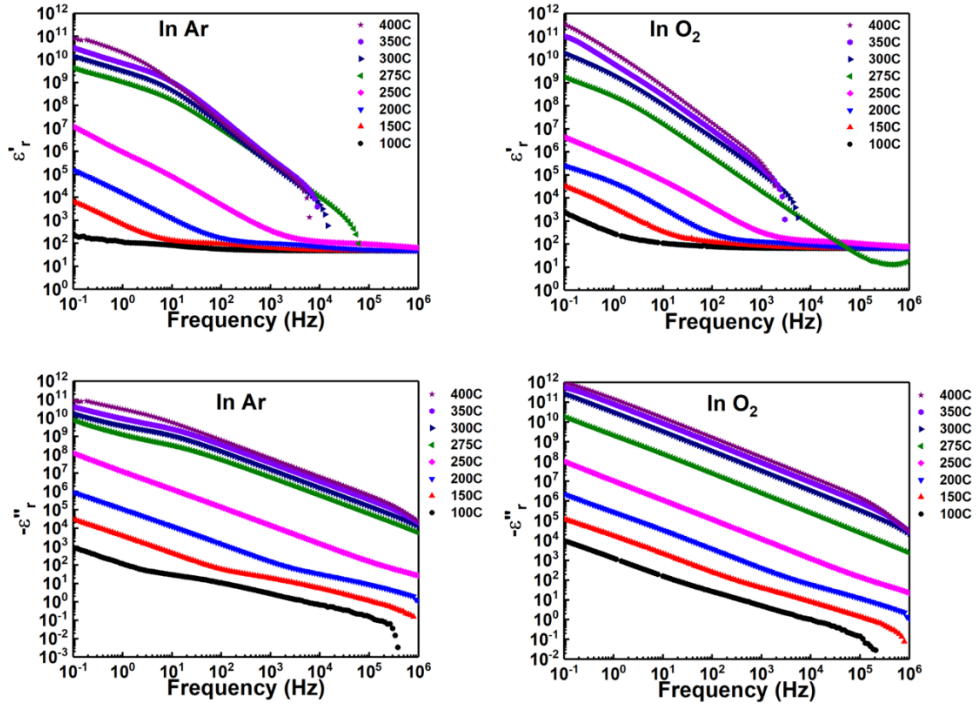

Figure 9. Temperature-dependent real and imaginary relative dielectric constant ε_r - f curves of α-Na_2O_2.

The fact that the conductivity of α-Na_2O_2 was enhanced in an O_2 atmosphere over an Ar atmosphere suggests that the ionic conducting mechanism is strongly related to the oxygen anions. Two possible charge-carriers can be identified, namely sodium vacancies V_{Na}' or interstitial oxygen O_i' or $(O_2)_i''$, using the Kröger-Vink notation. The enhanced conduction in an oxygen atmosphere can then be described by the mechanism

$$O_2 + 2e^- \rightarrow 2O_O^{\times} + 2V'_{Na} \qquad (1)$$

$$O_2 + 2e^- \rightarrow 2O'_i \; or \; O_2 + 2e^- \rightarrow (O_2)''_i \qquad (2)$$

Thus, the conductivity observed here could be caused either by Na^+ or O^-/O_2^{2-} ions. Yang and Siegel[15] have calculated the formation energy of several potential defects in α-Na_2O_2 and concluded that the formation of sodium vacancies is energetically preferred. The above structural analysis reveals that the O(2*e*) and Na(3*g*) atoms in the layer perpendicular to the *c* axis have higher thermal vibrations and thus might be expected to dominate the high ionic conduction/migration in the *a*-*b* plane. This expectation is consistent with the following observations. (a) The cell expands more in *a*-*b* plane than along *c* axis with increasing temperature as evident from the decrease in the *c*/*a* ratio as the temperature increases (Figure 4d). (b) As discussed above, the apparent shortening of the bond length *L* of O_2^{2-} peroxide ions at the 2*e* sites at $T \geqslant 250$ ºC, which are parallel to the *c* axis (Figure 5), could be explained by precession of the O–O dimers in the *a*-*b* plane. The conductivity increasing at $T \geqslant 250$ ºC might be a cooperative behavior of Na-O ions or charge carriers and a detailed study is planning in our further studies.

Conclusions

In summary, the crystal structures of Na_2O_2 were investigated using variable-temperature (from RT to 500 ºC) ND and syn-XRD measurements. A phase transition from α-Na_2O_2 to β-Na_2O_2 is observed in the ND profiles measured >400 ºC and the crystal structure of β-Na_2O_2 was determined from ND data measured at 500 ºC. α-Na_2O_2 has a hexagonal $P\bar{6}2m$ (No 189) structure and β-Na_2O_2 has a tetragonal $I4_1/acd$ (No. 142) structure, and is isostructural to tetragonal Na_2C_2. A re-alignment/rotation of O_2^{2-} groups occurs during the phase transition. The coordinate number (CN) of the O_2^{2-} dimer is nine and that of Na^+ is six (involving five O_2^{2-} dimers) in α-Na_2O_2; while the CN of O_2^{2-} dimer is eight and that of Na^+ is six (involving four O_2^{2-} dimers) in β-Na_2O_2. In α-Na_2O_2, the average Na-O and O-O bond lengths are 2.368(1) Å and 1.542(2) Å. In β-Na_2O_2, the average Na-O and O-O bond lengths are 2.442(3) Å and 1.557(8) Å, which are longer than that of α-Na_2O_2. The average cell parameter thermal expansion coefficients of α-Na_2O_2 is $a = 2.98\times10^{-5}$ K^{-1}, $c = 2.89\times10^{-5}$ K^{-1} and $V = 8.96\times10^{-5}$ K^{-1} up to 400 ºC and a ~10% volume expansion occurs during the phase transition from α-Na_2O_2 to β-Na_2O_2.

DFT calculations reveal that α-Na_2O_2 has an indirect band gap E_g(i) = 1.83 eV (**Γ→A**) and a direct band gap E_g(d) = 2.28 eV (**A→A**). The change in structure results in an increase in both the indirect band gap E_g(i) and direct band gaps to 2.56 eV and E_g(d) is 2.65 eV respectively in β-Na_2O_2. Impedance analysis from RT to 400 ºC revealed a significant enhancement of conductivity above 275 ºC under both an O_2 and Ar atmosphere, although the total conductivity was greater under O_2. We confirmed, by dielectric analysis, that this enhanced conductivity is dominated by ionic conduction. The atoms O(2*e*) and Na(3*g*) in the layer perpendicular to *c*

axis, with the highest thermal vibrations, probably dominate this high ionic conduction/migration especially at $T \geq 275$ ºC.

Acknowledgements

This work was supported by the Fundamental Research Funds for the Central Universities (G2019KY05103/ G2019KY05103), Natural Science Foundation of Shaanxi Province (2020JM-117) China, and the Australian Research Council – Discovery Projects scheme (CHW, BJK, CDL). This research was undertaken, in part, on the Powder Diffraction beamline at the Australian Synchrotron.

Supporting Information. Supplemental variable temperature diffraction patterns of Na_2O_2, Pawley/Rietveld - refinement profiles against ND data at 450°C and 500°C, impedance spectra, Band structure of α-Na_2O_2 and β-Na_2O_2 from DFT calculations and refined CIF files (CSD 2020976-2020982).

References

(1) Soloveichik, G. L., Battery technologies for large-scale stationary energy storage, *Annu Rev Chem Biomol Eng*, **2011,** 2, 503-527.
(2) Ellis, B. L.; Nazar, L. F., Sodium and sodium-ion energy storage batteries, *Current Opinion in Solid State and Materials Science*, **2012,** 16, 168-177.
(3) Adelhelm, P.; Hartmann, P.; Bender, C. L.; Busche, M.; Eufinger, C.; Janek, J., From lithium to sodium: cell chemistry of room temperature sodium-air and sodium-sulfur batteries, *Beilstein J. Nanotech.*, **2015,** 6, 1016-1055.
(4) Wriedt, H. A., The Na-O (Sodium-Oxygen) System, *Bull. Alloy Phase Diagr.*, **1987,** 8, 234-246.
(5) Zintl, E.; Harder, A.; Dauth, B., The atomic structure of the oxides, sulphides, selenides and tellurides of lithium, sodium and kalium, *Z. Elektrochem.*, **1934,** 40, 588-593.
(6) Tallman, R. L.; Margrave, J. L.; Bailey, S. W., THE CRYSTAL STRUCTURE OF SODIUM PEROXIDE, *J. Am. Chem. Soc.*, **1957,** 79, 2979-2980.
(7) Tallman, R. L.; Margrave, J. L., EVIDENCE FOR 2 NEW CRYSTALLINE FORMS OF SODIUM PEROXIDE, *J. Inorg. Nucl. Chem.*, **1961,** 21, 40-44.
(8) Bruesch, P.; Bosch, M.; Kanzig, W.; Ziegler, M.; Buhrer, W., LATTICE-DYNAMICS OF PHASE-1, PHASE-2, AND PHASE-3 OF SODIUM HYPEROXIDE NAO2, *Phys. Status. Solidi. B*, **1976,** 77, 153-164.
(9) Ziegler, M.; Rosenfeld, M.; Kanzig, W.; Fischer, P., STRUCTURAL EXAMINATION OF ALKALINE HYPEROXIDES, *Helv. Phys. Acta*, **1976,** 49, 57-90.
(10) Klein, W.; Armbruster, K.; Jansen, M., Synthesis and crystal structure determination of sodium ozonide, *Chem. Commun.*, **1998**, 707-708.
(11) Bi, X.; Wang, R.; Amine, K.; Lu, J., A Critical Review on Superoxide-Based Sodium-Oxygen Batteries, *Small Methods*, **2019,** 3.
(12) Bi, X.; Wang, R.; Ma, L.; Zhang, D.; Amine, K.; Lu, J., Sodium Peroxide Dihydrate or Sodium Superoxide: The Importance of the Cell Configuration for Sodium-Oxygen Batteries, *Small Methods*, **2017,** 1.
(13) Bender, C. L.; Schroeder, D.; Pinedo, R.; Adelhelm, P.; Janek, J., One- or Two-Electron Transfer? The Ambiguous Nature of the Discharge Products in Sodium-Oxygen Batteries, *Angew. Chem. Int. Edit.*, **2016,** 55, 4640-4649.
(14) Hartmann, P.; Bender, C. L.; Sann, J.; Duerr, A. K.; Jansen, M.; Janek, J.; Adelhelm, P., A comprehensive study on the cell chemistry of the sodium superoxide (NaO_2) battery, *Phys. Chem. Chem. Phys.*, **2013,** 15, 11661-11672.
(15) Yang, S.; Siegel, D. J., Intrinsic Conductivity in Sodium–Air Battery Discharge Phases: Sodium Superoxide vs Sodium Peroxide, *Chem. Mater.*, **2015,** 27, 3852-3860.

(16) Sun, B.; Pompe, C.; Dongmo, S.; Zhang, J.; Kretschmer, K.; Schroeder, D.; Janek, J.; Wang, G., Challenges for Developing Rechargeable Room-Temperature Sodium Oxygen Batteries, *Adv. Mater. Technol.*, **2018,** 3.
(17) Araujo, R. B.; Chakraborty, S.; Ahuja, R., Unveiling the charge migration mechanism in Na_2O_2: implications for sodium-air batteries, *Phys. Chem. Chem. Phys.*, **2015,** 17, 8203-8209.
(18) Dunst, A.; Sternad, M.; Wilkening, M., Overall conductivity and NCL-type relaxation behavior in nanocrystalline sodium peroxide Na 2 O 2 —Consequences for Na-oxygen batteries, *Mat. Sci. Eng. B*, **2016,** 211, 85-93.
(19) Philipp, M.; Lunghammer, S.; Hanzu, I.; Wilkening, M., Partial electronic conductivity of nanocrystalline Na_2O_2, *Mater. Res. Express*, **2017,** 4.
(20) Wallwork, K. S.; Kennedy, B. J.; Wang, D., The high resolution powder diffraction beamline for the Australian Synchrotron. In *Synchrotron Radiation Instrumentation, Pts 1 and 2*, Choi, J. Y.; Rah, S., Eds. 2007; Vol. 879, pp 879-882.
(21) Avdeev, M.; Hester, J. R., ECHIDNA: a decade of high-resolution neutron powder diffraction at OPAL, *J. Appl. Crystallogr.*, **2018,** 51, 1597-1604.
(22) Coelho, A. A.; Evans, J. S. O.; Evans, I. R.; Kern, A.; Parsons, S., The TOPAS symbolic computation system, *Powder Diffr.*, **2011,** 26, S22-S25.
(23) Evans, J. S. O., Advanced Input Files & Parametric Quantitative Analysis Using Topas. In *Extending the Reach of Powder Diffraction Modelling by User Defined Macros*, Scardi, P.; Dinnebier, R. E., Eds. 2010; Vol. 651, pp 1-9.
(24) Petricek, V.; Dusek, M.; Palatinus, L., Crystallographic Computing System JANA2006: General features, *Zeitschrift Fur Kristallographie-Crystalline Materials*, **2014,** 229, 345-352.
(25) Momma, K.; Izumi, F., VESTA 3 for three-dimensional visualization of crystal, volumetric and morphology data, *J. Appl. Crystallogr.*, **2011,** 44, 1272-1276.
(26) Milman, V.; Refson, K.; Clark, S. J.; Pickard, C. J.; Yates, J. R.; Gao, S. P.; Hasnip, P. J.; Probert, M. I. J.; Perlov, A.; Segall, M. D., Electron and vibrational spectroscopies using DFT, plane waves and pseudopotentials: CASTEP implementation, *J. Mol. Struc-theochem*, **2010,** 954, 22-35.
(27) Perdew, J. P.; Ruzsinszky, A.; Csonka, G. I.; Vydrov, O. A.; Scuseria, G. E.; Constantin, L. A.; Zhou, X.; Burke, K., Restoring the density-gradient expansion for exchange in solids and surfaces, *Phys. Rev. Lett.*, **2008,** 100.
(28) Sears, V. F., Neutron scattering lengths and cross sections, *Neutron News*, **1992,** 3, 26-37.
(29) Murphy, G. L.; Wang, C.-H.; Beridze, G.; Zhang, Z.; Kimpton, J. A.; Avdeev, M.; Kowalski, P. M.; Kennedy, B. J., Unexpected Crystallographic Phase Transformation in Nonstoichiometric $SrUO_{4-x}$: Reversible Oxygen Defect Ordering and Symmetry Lowering with Increasing Temperature, *Inorg. Chem.*, **2018,** 57, 5948-5958.
(30) Hemmersbach, S.; Zibrowius, B.; Ruschewitz, U., Na_2C_2 and K_2C_2: Synthesis, crystal structure, and spectroscopic properties, *Z. Anorg. Allg. Chem.*, **1999,** 625, 1440-1446.
(31) Federicci, R.; Hole, S.; Popa, A. F.; Brohan, L.; Baptiste, B.; Mercone, S.; Leridon, B., $Rb_2Ti_2O_5$: Superionic conductor with colossal dielectric constant, *Phys. Rev. Mater.*, **2017,** 1.
(32) Seidl, A.; Gorling, A.; Vogl, P.; Majewski, J. A.; Levy, M., Generalized Kohn-Sham schemes and the band-gap problem, *Phys. Rev. B*, **1996,** 53, 3764-3774.
(33) Xiao, H.; Tahir-Kheli, J.; Goddard, W. A., III, Accurate Band Gaps for Semiconductors from Density Functional Theory, *J. Phys. Chem. Lett.*, **2011,** 2, 212-217.

For Table of Contents Only

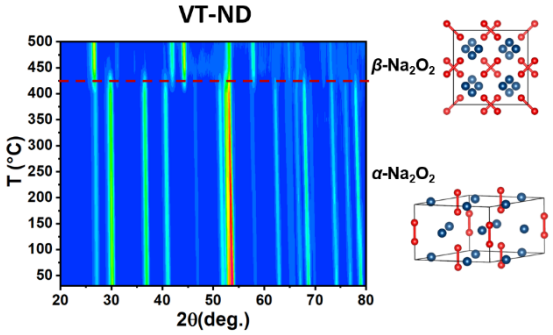

Phase transition from α-Na_2O_2 ($P\bar{6}2m$) to β-Na_2O_2 ($I4_1/acd$) occurs above 400 ºC.

A phase transition from hexagonal α-Na_2O_2 [$P\bar{6}2m$ (No. 189)] to tetragonal β-Na_2O_2 [$I4_1/acd$ (No. 142)] is observed in neutron diffraction measurements above 400 ºC. The thermal expansion coefficients of α-Na_2O_2 is $a = 2.98\times10^{-5}$ K^{-1}, $c = 2.89\times10^{-5}$ K^{-1} and $V = 8.96\times10^{-5}$ K^{-1} up to 400 ºC and a ~10% volume expansion occurs during the phase transition from α-Na_2O_2 to β-Na_2O_2 due to the re-alignment/rotation of O_2^{2-} groups.